Structure of the new iron(II) oxalate potassium salt K2Fe[(C2O4)2(H2O)2]×0.18H2O

S. Amanchar, T. Schweitzer, T. Mazet, B. Malaman, L. V. B. Diop, M. Francois

Acta Cryst B
STRUCTURAL SCIENCE
CRYSTAL ENGINEERING
MATERIALS

ISSN 2052-5206

Structure of the new iron(II) oxalate potassium salt $K_2Fe[(C_2O_4)_2(H_2O)_2]\cdot 0.18H_2O$

Sara Amanchar,* Thierry Schweitzer, Thomas Mazet, Bernard Malaman, Leopold V. B Diop and Michel Francois

Université de Lorraine, CNRS, IJL, F-54000 Nancy, France. *Correspondence e-mail: sara.aarras@univ-lorraine.fr

Received 24 January 2023
Accepted 24 May 2023

Edited by R. Černý, University of Geneva, Switzerland

Keywords: metal–organic framework; iron(II) oxalate; crystal structure.

CCDC reference: 2265160

Supporting information: this article has supporting information at journals.iucr.org/b

The discovery of a new Fe^{II} oxalate framework of composition $K_2Fe[(C_2O_4)_2(H_2O)_2]\cdot 0.18H_2O$ is reported. Its crystal structure was solved by means of single crystal and powder X-ray diffraction. The new organic–inorganic hybrid compound crystallizes in the orthorhombic space group $Pca2_1$ with unit-cell parameters: a = 12.0351 (4) Å, b = 15.1265 (5) Å, c = 10.5562 (4) Å. This crystal structure, containing eight chemical formula, consists of a succession of $FeO_4(H_2O)_2$ octahedra and K^+ cations growing along b direction. Magnetization measurements indicate that the title compound is paramagnetic over the investigated temperature range (2–300 K). Both magnetization and ^{57}Fe Mössbauer data indicate that Fe^{2+} is in a high-spin state.

1. Introduction

Coordination networks (CNs), such as metal–organic frameworks (MOFs), have emerged in the past decades as promising materials with a wide range of potential applications including catalysis, drug delivery, separation, molecular recognition, gas storage and magnetism among others (Li *et al.*, 1999). These hybrid solids are built from the assembly of inorganic subunits and organic ligands. Such a combination has given rise to wide structural diversity and fascinating physical properties. The geometry of the constituent metallic ions, together with the adaptable nature of the organic linkers and their assortment of coordination modes, yield a variety of topologies and diverse architectures that can be achieved by chemical design (Mínguez Espallarga & Coronado *et al.*, 2018). Besides this structural flexibility, the crystalline hybrid organic–inorganic materials display other interesting properties resulting from the various ways in which numerous functionalities can be integrated into these solids. In particular, electrical, optical or magnetic properties can stem from MOFs by properly selecting the metal nodes, the organic ligands and the manner in which they are linked in the hybrid material. In other words, hybrid materials offer the opportunity to finely tune the physical properties by choosing the appropriate components that these compounds are made of.

The discovery of bimetallic magnets $A[M^{II}M^{III}(ox)_3]$ (M^{II} = Mn, Fe, Co, Ni, Cu; M^{III} = Cr, Fe; ox = oxalate; A = organic or organometallic cation) has triggered a spectacular surge of interest (Coronado *et al.*, 1999) in the search for novel magnetic CNs. The oxalate ligand is widely employed in the design of a very large variety of homo- and hetero-transition

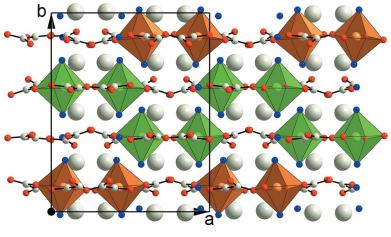

metal based hybrid compounds. The reason of this extensive use is twofold:

(i) the predominance of its stiff bis-chelating bridging mode offering some degree of predictability concerning the structural features of the resulting metal oxalate networks (García-Couceiro *et al.*, 2006).

(ii) its ability to mediate electronic phenomena between metal ions providing materials with a broad range of magnetic behaviors.

The shape of the templating counterions or the characteristics of the supplementary organic linkers employed to complete the metal coordination sphere determine basically the dimensionality and topology of transition metal oxalate networks. When magnetic frustration is induced by the topology of the crystal lattice, it is expected to lead to highly degenerate ground states with short-range spin–spin correlations and exotic phenomena such as spin ice, spin glass and spin liquid phases can emerge (Moessner & Ramirez, 2006; Lhotel *et al.*, 2013). In the case of spin ice, disorder persists even at low temperatures, creating a state with a high degeneracy of possible configurations. The magnetic ions form a network of interlinked tetrahedra, where the spins can point either inwards or outwards. As for spin liquid, the disorder is dynamic, with spins fluctuating and interacting in a disordered manner, even at low temperatures. This results in a state with short-range correlations, but without long-range order. Spin glass exhibits a different behavior. Below a certain freezing temperature, there is a long-range order that emerges, although it is non-periodic and stems from magnetic frustration. Within the various potential low-dimensional spin-frustrated materials and geometrically frustrated magnetic systems, CNs exhibit unique advantages in structure modulation (Zhao *et al.*, 2015). It is noteworthy that oxalate linkers have been exploited in the search for new kagome lattice systems (Lhotel *et al.*, 2013) and have been employed previously in the preparation of honeycomb magnets (Coronado *et al.*, 1999; Tamaki *et al.*, 1992).

Interestingly, an iron(II) oxalate framework of composition $[NH_4]_2[Fe^{II}(C_2O_4)_2]\cdot H_2O$ was most recently synthetized successfully via solvent-free approach (Li *et al.*, 2015). This new homometallic hybrid compound possesses a pillar-layer architecture with a **hms** topology which is well known to generate magnetic frustration. In the framework of our search for new and model magnetic compounds exhibiting kagome topology and magnetic frustration, we have selected the $[NH_4]_2[Fe^{II}(C_2O_4)_2]\cdot H_2O$ system in the Cambridge Structural Database (CSD; Groom *et al.*, 2016) database via *Topcryst* (Blatov *et al.*, 2004). This choice is motivated by the simplicity of its useful composition and thus appearing as a good model compound, and its topology which is described as kag, 6/3/h13; sqc249 in cluster representation of valence-bonded compounds (RINGS>5) and **hms** in standard representation of coordination compounds and valence-bonded MOFs.

Guided by these motivations, we set out to explore the preparation of the iron(II) oxalate compound $K_2[Fe^{II}(C_2O_4)_2]\cdot 0.18H_2O$ isotype of $[NH_4]_2[Fe^{II}(C_2O_4)_2]\cdot H_2O$ (Li *et al.*, 2015) and $K_4Na_2[Fe^{II}(C_2O_4)_2]_3\cdot 2H_2O$ (Wang *et al.*, 2014) by replacing the NH_4^+ cation with K^+ in a solvent-free synthesis. It should be emphasized that the synthesis of $[NH_4][Fe^{II}(C_2O_4)_2]$ was performed without solvent at 140°C. By employing similar synthetic routes under the same experimental conditions, the expected anhydrous phase $K_2[Fe^{II}(C_2O_4)_2]$ is not obtained, even upon heating up to 200°C. By contrast, a new hydrated phase appeared at room temperature during the mixing of the powders without solvent, and therefore, it is this novel $K_2[Fe(C_2O_4)_2(H_2O)_2]\cdot 0.18H_2O$ compound which is reported in the present article.

2. Experimental

2.1. Synthesis and crystallization

Iron (II)-based compound $K_2[Fe(C_2O_4)_2(H_2O)_2]\cdot 0.18H_2O$ (**1**) was entirely synthesized in a glove box under N_2-5%H_2 reductive atmosphere to avoid oxidization of Fe^{II} to Fe^{III}. The two starting powders of monohydrate di-potassium oxalate ($K_2C_2O_4\cdot H_2O$, Aldrich, 7 mmol) and dichloro tetrahydrate iron(II) ($FeCl_2\cdot 4H_2O$, Aldrich, 9 mmol) were finely ground in an agate mortar for 20 min to obtain a homogeneous mixture which had the texture of a paste.

The following chemical reaction occurs at room temperature during mixing and corresponds to a change in color from greenish, the ferrous chloride, to orange, the color of the resulting compound.

$$2K_2C_2O_4 + H_2O + Fe^{II}Cl_2 + 4H_2O = K_2[Fe^{II}(C_2O_4)_2(H_2O)_2]\cdot 0.18H_2O\ (\mathbf{1}) + 2KCl + 3.82H_2O$$

The composition of **1** was established afterwards. The paste was dried at room temperature in the glove box for three days and then analyzed using powder X-ray diffraction. The orange powder was washed with demineralized water in the glove box. The filtrate was recovered and then evaporated into the glove box by heating to 60°C until completely dried. Orange crystals were formed mixed with colorless ones of KCl. Further X-ray diffraction analysis indicated orange crystals corresponded to the phase $K_2[Fe(II)(C_2O_4)_2(H_2O)_2]\cdot 0.18H_2O$.

2.2. Powder X-ray diffraction

An X-ray diffraction pattern of the orange powder (before washing with water) was recorded from 10 to 80° (2θ) with angular steps of 0.01° over 2 h at room temperature using a Bruker D8-Advance diffractometer with a copper anticathode and Ge(111)-monochromator (λCu $K\alpha 1$ = 1.54056 Å), in a classical Bragg–Brentano reflection geometry (θ–2θ).

The raw X-ray powder diffraction pattern is shown in Fig. S1. The peaks of the KCl phase (space group: $Fm\bar{3}m$) are indicated by asterisks. The phase **1** peaks do not match any known compounds.

Rietveld refinement was performed on the orange powder with the structural models of **1** obtained from single crystals (see hereafter) and the structure of KCl ($Fm\bar{3}m$, a = 6.296 Å) using *Fullprof_Suite* (Rodríguez-Carvajal, 2011).

Table 1
Experimental details.

Crystal data	
Chemical formula	$K_2[Fe^{II}(C_2O_4)_2(H_2O)_2]\cdot 0.18H_2O$
M_r	344.95
Crystal system, space group	Orthorhombic, $Pca2_1$
Temperature (K)	296
a, b, c (Å)	12.0351 (4), 15.1265 (5), 10.5562 (4)
V (Å^3)	1921.74 (12)
Z	8
Radiation type	Mo $K\alpha$
μ (mm^{-1})	2.48
Crystal size (mm)	0.27 × 0.19 × 0.18
Data collection	
Diffractometer	Bruker APEX-II QUAZAR CCD
Absorption correction	Multi-scan (*SADABS*)
No. of measured, independent and observed [$I > 2\sigma(I)$] reflections	50068, 11933, 10385
R_{int}	0.026
$(\sin\theta/\lambda)_{max}$ (Å^{-1})	0.909
Refinement	
$R[F^2 > 2\sigma(F^2)]$, $wR(F^2)$, S	0.037, 0.100, 1.08
No. of reflections	11933
No. of parameters	318
No. of restraints	1
H-atom treatment	H-atom parameters not located
$\Delta\rho_{max}$, $\Delta\rho_{min}$ (e Å^{-3})	2.28, −1.03
Absolute structure	Refined as an inversion twin
Absolute structure parameter	0.512 (13)

Computer programs: *SADABS* (Bruker, 2004), *SHELXL2018/3* (Sheldrick, 2015).

Table 2
Selected interatomic distances (Å) in $K_2[Fe^{II}(C_2O_4)_2(H_2O)_2]\cdot 0.18H_2O$.

Fe1···O*W*2	2.078 (2)	K3···O1*C*	2.728 (2)
Fe1···O*W*1	2.080 (2)	K3···O2*C*^{viii}	2.770 (2)
Fe1···O3*B*	2.109 (2)	K3···O4*A*^{xiv}	2.777 (2)
Fe1···O1*B*^{i}	2.129 (2)	K3···O1^{iv}	2.896 (2)
Fe1···O4*A*	2.174 (2)	K3···O2*B*^{iii}	2.896 (2)
Fe1···O1*A*	2.174 (2)	K3···O3*B*^{iv}	2.947 (2)
	Av. 2.124 (1)	K3···O4*D*^{vi}	2.972 (2)
Fe2···O*W*3^{v}	2.0926 (19)	K3···O3*C*^{viii}	3.205 (2)
Fe2···O*W*4	2.094 (2)	CN = 7	Av. 2.855
Fe2···O1*D*	2.103 (2)	K4—O2*A*	2.711 (2)
Fe2···O3*D*^{vi}	2.124 (2)	K4···O2*B*^{xv}	2.736 (2)
Fe2···O1*C*	2.127 (2)	K4···O1*A*^{x}	2.737 (2)
Fe2···O4*C*	2.214 (2)	K4···O4*A*^{iv}	2.835 (2)
	Av. 2.126 (1)	K4···O1*B*^{iii}	2.856 (2)
K1···O3*C*	2.736 (2)	K4···O3*B*^{iii}	2.922 (2)
K1···O4*C*^{ix}	2.7513 (18)	K4···O4*B*^{x}	2.959 (2)
K1···O1*C*^{x}	2.785 (2)	K4···O*W*2^{iv}	3.375 (3)
K1···O1*D*^{ix}	2.807 (2)	CN = 7	Av. 2.8222
K1···O4*D*^{xi}	2.828 (2)	C1*A*—O2*A*	1.245 (3)
K1···O3*D*^{ix}	2.940 (2)	C1*A*—O1*A*	1.267 (3)
K1···O2*D*^{xii}	2.975 (2)	C1*A*—C2*A*	1.544 (3)
K1···O*W*3^{xiii}	3.086 (2)	C2*A*—O3*A*	1.243 (3)
CN = 7	Av. 2.863	C2*A*—O4*A*	1.267 (3)
K2···O2*D*	2.683 (2)	C1*B*—O4*B*	1.240 (3)
K2···O3*A*^{xiv}	2.694 (2)	C1*B*—O3*B*	1.273 (3)
K2···O4*B*^{ii}	2.740 (2)	C1*B*—C2*B*	1.561 (3)
K2···O1*A*^{ii}	2.794 (2)	C2*B*—O2*B*	1.248 (3)
K2···O4*C*^{vi}	2.871 (2)	C2*B*—O1*B*	1.264 (3)
K2···O1*D*^{vi}	2.926 (2)	C1*C*—O2*C*	1.237 (3)
K2···O3*D*^{vi}	2.999 (2)	C1*C*—O1*C*	1.276 (3)
K2···O*W*4^{vi}	3.137 (2)	C1*C*—C2*C*	1.547 (3)
K2···O*W*1^{ii}	3.339 (2)	C2*C*—O3*C*	1.251 (3)
CN = 7	Av. 2.815	C2*C*—O4*C*	1.264 (3)
		C1*D*—O4*D*	1.248 (3)
		C1*D*—O3*D*	1.269 (3)
		C1*D*—C2*D*	1.560 (3)
		C2*D*—O2*D*	1.242 (3)
		C2*D*—O1*D*	1.269 (3)
		O*W*1—O*W*5	1.781 (11)
		O*W*2—O*W*6	1.736 (10)
		O*W*3—O*W*5	1.632 (11)
		O*W*4—O*W*6	1.743 (10)

Symmetry code(s): (i) $-x+\frac{3}{2}, y, z-\frac{1}{2}$; (ii) $x+\frac{1}{2}, -y+1, z$; (iii) $-x+1, -y+1, z-\frac{1}{2}$; (iv) $x-\frac{1}{2}, -y+1, z$; (v) $x, y+1, z$; (vi) $-x+\frac{3}{2}, y, z+\frac{1}{2}$; (vii) $x+\frac{1}{2}, -y+2, z$; (viii) $-x+\frac{1}{2}, y, z+\frac{1}{2}$; (ix) $x-\frac{1}{2}, -y+2, z$; (x) $-x+\frac{1}{2}, y, z-\frac{1}{2}$; (xi) $x-1, y, z$; (xii) $-x+1, -y+2, z-\frac{1}{2}$; (xiii) $-x+\frac{1}{2}, y+1, z-\frac{1}{2}$; (xiv) $-x+1, -y+1, z+\frac{1}{2}$; (xv) $x-\frac{1}{2}, -y+1, z-1$.

2.3. Single-crystal data collection and structure determination

A suitable orange single crystal was selected under a binocular and then used for collecting X-ray diffraction data at 100 K. It was glued to a MiTeGen MicroLoops mounted on an Bruker APEX II area detector four-circle diffractometer. Intensity data sets were collected using Mo $K\alpha$ (λ = 0.71073 Å) microsource radiation through the program *APEX2* to establish the data collection strategy with a series of 1.0° scans in ω and φ (Bruker, 2004). The collection of intensity data as well as unit-cell refinement and data reduction were carried out using the *APEX2* (Bruker, 2004) program. An empirical absorption correction based on symmetry equivalent reflections in orthorhombic Laue group *mmm* was applied using the *SADABS* program (Krause *et al.*, 2015). Structural solution was found in the orthorhombic crystal system with unit-cell parameters a = 12.0351 (4) Å, b = 15.1265 (5) Å, c = 10.5562 (4) Å, V = 1921.74 (12) Å^3 in the noncentrosymmetric space group $Pca2_1$, according to the automated search for space group available in *JANA2006* software (Petříček *et al.*, 2014).

The structure of this compound was solved with the charge flipping method implemented in *JANA*, and refined by a full-matrix least-squares technique with *SHELXL2014* (Sheldrick, 2008) with anisotropic displacement parameters for all non H-atoms. Water H atoms were not located. The drawings were made with *DIAMOND* program (Brandenburg & Putz, 1999). The main crystallographic data and refinement parameters are presented in Table 1. The final fractional atomic coordinates and equivalent isotropic displacement parameters are given in Table S1. Bond distances and angles calculated from the final atomic coordinates, as well as probable hydrogen bonds, are given in Tables 2 and 3, respectively.

2.4. ^{57}Fe Mössbauer spectroscopy

The ^{57}Fe Mössbauer spectrum was recorded in transmission geometry using a constant-acceleration spectrometer with a 25 mCi ^{57}Co source in a Rh matrix. The velocity scale was calibrated with a metallic iron foil at room temperature. The data were analyzed with a least-square fitting program assuming Lorentzian peaks (Le Caër, private communication). Isomer shifts are given with respect to α-Fe at room temperature.

Table 3
Hydrogen-bonding geometry (Å, °).

D	*A*	Distances	*A*···*D*···*A*′	Angles
*OW*2	O2*A*	2.639 (3)	O2*A*···*OW*2···O2*B*	114.33 (6)
	O2*B*	2.767 (3)		
*OW*4	O3*A*	2.702 (3)	O3*A*···*OW*4···O4*B*	119.88 (8)
	O4*B*	2.760 (3)		
*OW*1	O2*C*	2.681 (3)	O2*C*···*OW*1···O2*D*	116.20 (7)
	O2*D*	2.728 (3)		
*OW*3	O3*C*	2.678 (3)	O3*C*···*OW*3···O4*D*	120.09 (9)
	O4*D*	2.785 (3)		

2.5. Magnetic susceptibility

The thermal variation (2–300 K) of the magnetic susceptibility was measured with a physical property measurement system (PPMS) from Quantum Design upon cooling in a magnetic field of 10 kOe.

3. Results and discussion

3.1. Structural description

The organic–inorganic hybrid material $K_2[Fe^{II}(C_2O_4)_2(H_2O)_2]\cdot 0.18H_2O$ crystallizes in the noncentrosymmetric orthorhombic space group $Pca2_1$ with unit-cell parameters a = 12.0351 (4) Å, b = 15.1265 (5) Å, c = 10.5562 (4) Å, V = 1921.74 (12) Å^3, D_x = 2.385 g cm^{-3}.

The asymmetric unit of the structure is depicted in Fig. 1. It contains two sites for iron atoms (Fe1 and Fe2) in irregular O-octahedral coordination, four independent oxalate molecules denoted as Ox_*a*, Ox_*b*, Ox_*c* and Ox_*d*, four sites for potassium atoms (K1–K4) and four sites for coordinating water molecules (O*W*1–O*W*4). Sites O*W*5 and O*W*6 are occupied by inserted water molecules, each with an occupancy factor of 18%. Fig. S3 displays the resulting plot of the thermogravimetric analysis conducted on the powder sample $K_2[Fe^{II}(C_2O_4)_2(H_2O)_2]\cdot 0.18H_2O$ + 2KCl. The thermogravimetric results are consistent with the crystallographic data reported in Table 1.

For the two iron sites, Fe1 and Fe2, the first six neighboring oxygen atoms come from three oxalate molecules, one of which is chelating and the other two are bridging, and two water molecules.

Coordination of iron(II). In the equatorial plane of the octahedron $Fe1O_4(H_2O)_2$ the coordination is ensured by two oxygen atoms of the Ox_*A* group (O1*A* and O4*A*) and by two other oxygen atoms O1*B* and O3*B* of the two groups Ox_*B* and Ox_*B*′ connected by axis 2_1 parallel to the *c* direction. The two oxygen atoms of the two water molecules O*W*1 and O*W*2 form the apices of the octahedron. The oxygen atoms O2*A*, O3*A*, O2*B* and O4*B* are not connected to the metal. For the octahedron $Fe2O_4(H_2O)_2$ the situation is identical. In the equatorial plane the coordination is ensured by the two oxygen atoms of Ox_*C* (O1*C* and O4*C*) and two other oxygen atoms O1*D* and O3*D* of Ox_*D* and Ox_*D*′. The two oxygen atoms of two water molecules O*W*3 and O*W*4 form the apex of the octahedron. The oxygen atoms O2*C*, O3*C*, O2*D* and O4*D* are not connected to the metal.

The Fe–O distances range from 2.078 (2) to 2.174 (2) Å (av. 2.124 Å) and from 2.093 (2) to 2.214 (2) Å (av. 2.126 Å) for Fe1 and Fe2, respectively. These distances are in accordance with the sum of the ionic radii extracted from the Shannon table [rFe^{2+} (HS, CN = 6) + rO^{2-} = 0.78 + 1.40 = 2.18 Å] (Shannon & Prewitt, 1969; Shannon, 1976).

Coordination of K. The coordination polyhedra around the four K sites in the structure of $K_2[Fe^{II}(C_2O_4)_2(H_2O)_2]\cdot 0.18H_2O$ are represented in Fig. 2 and K–O distances are reported in Table 2.

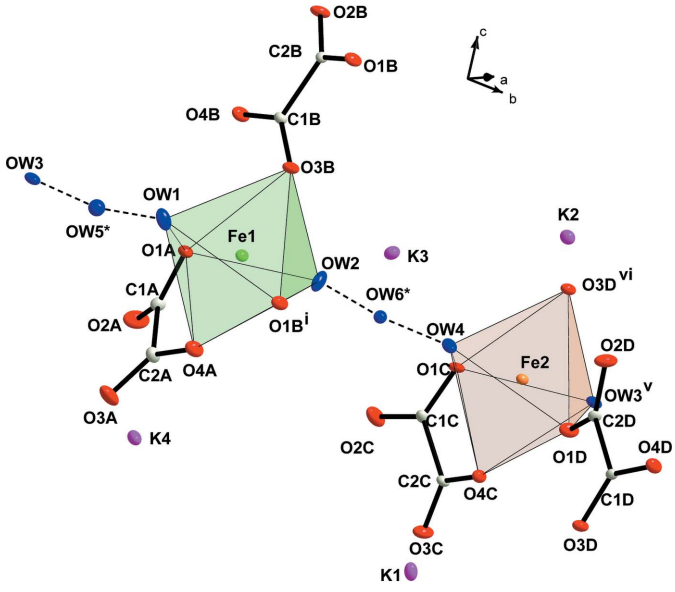

Figure 1
Asymmetric unit of $K_2[Fe^{II}(C_2O_4)_2(H_2O)_2]\cdot 0.18H_2O$. The superscript * indicates the residual ($0.18H_2O$/f.u) disordered water molecules.

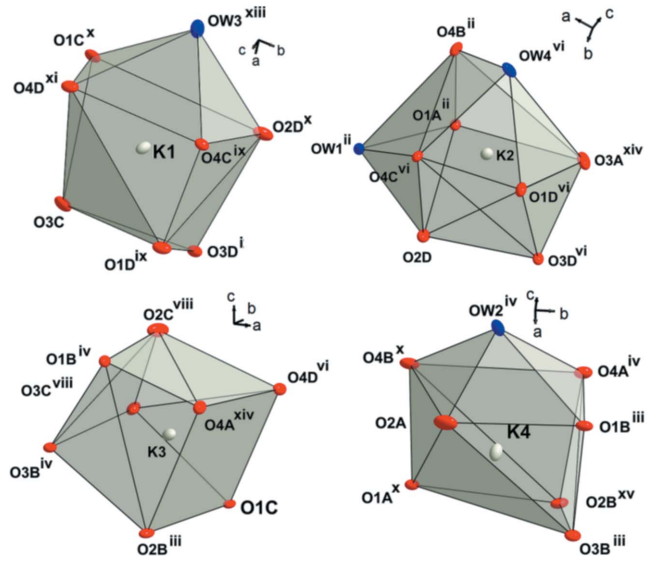

Figure 2
Local environment of potassium atoms in $K_2[Fe^{II}(C_2O_4)_2(H_2O)_2]\cdot 0.18H_2O$. Displacement ellipsoids are drawn at 75% probability level.

The distances K···O_{ox} range from 2.683 (2) to 3.205 (2) Å and K···O*W* from 3.086 (2) to 3.375 (3) Å. Due to the low local symmetry, the polyhedron do not present simple forms. Considering a coordination number of seven, the mean distances K–O_{ox} for each site K1–K4 are, respectively, 2.863 (2), 2.815 (2), 2.855 (2) and 2.822 (2) Å. These distances are in accordance with the sum of the ionic radius extracted from the Shannon table [rK^{+} (CN = 7) + rO^{2-} = 1.46 Å + 1.40 Å = 2.86 Å] (Shannon & Prewitt, 1969; Shannon, 1976).

The structure of $K_2[Fe^{II}(C_2O_4)_2(H_2O)_2]\cdot 0.18H_2O$ develops along the *b* axis by a succession of planes composed of octahedra $FeO_4(H_2O)_2$ and K^{+} cations, according to sequence $Fe(1)O_4(H_2O)_2$–K_2–$Fe(1)O_4(H_2O)_2$–K_2–$Fe(2)O_4(H_2O)_2$–K_2–$Fe(2)O_4(H_2O)_2$, as shown by the projection of the structure along the *c* axis (see Fig. 3).

The detail of a single plane containing the octahedra $Fe(1)O_6$ on the one hand and $Fe(2)O_6$ on the other hand is given in Fig. 4. In the *ac* plane the magnetic centers Fe1 are linked together by the oxalate molecules Ox_*D* so that zigzag chains run along the *c* axis. Fe1 centers are very far apart (Fe1···Fe1 = 6.749 Å) because they are separated by four atoms along the only possible magnetic pathway Fe1–O1*B*–C2*B*–C1*B*–O3*B*–Fe1. The same is true for Fe2 with the Fe2–O1*D*–C2*D*–C1*D*–O3*D*–Fe2 pathway. The atomic planes containing Fe1 and Fe2 look very similar. In reality, the length of the unit-cell parameter *b* = 15.1265 (5) Å reflects a superstructure with a doubling of the unit cell in this direction. The superstructure is relatively subtle (systematic weak intensities of the order of thousandths of the most intense reflection 080 for reflection *hkl* with $k = 2n+1$) and not visible on the powder diffraction pattern which seems perfectly indexed in the half-cell with unit-cell parameters *a* = 7.6668 (3) Å *b* = 12.0845 (4) Å *c* = 10.5543 (5) Å, space group $Cmc2_1$ (see Fig. S1).

The zigzag chains are connected to each other in the plane (010) by hydrogen bonds between the coordinating water molecules (donor oxygen *D*) and the oxygen atoms of the oxalate groups (acceptor oxygen *A*) not bound to the metal. Analysis of the distances *D*···*A* makes it possible to clearly locate these hydrogen bonds (here each coordinating water molecule O*W*1–O*W*4 establishes two hydrogen bonds) which allow the cohesion of the structure in each plane, even if the hydrogen atoms of the water molecules could not be located.

For planes containing Fe1, these are the four hydrogen bonds O*W*2···O2*A*, O*W*2···O2*B*, O*W*4···O3*A* and O*W*4···O4*B*, for planes containing Fe2 these are the four hydrogen bonds O*W*1—H···O2*C*, O*W*1···O2*D*, O*W*3···O3*C* and O*W*3···O4*B* as indicated by the contact distances O···O between 2.639 (3) and 2.784 (3) Å reported in Table 3. The angles between the oxygen atoms of the donor water molecule and the two acceptor oxygen atoms range from 114.33 (6)° to 120.09 (9)°, which is fairly close to the angle of the water molecule (104.5°).

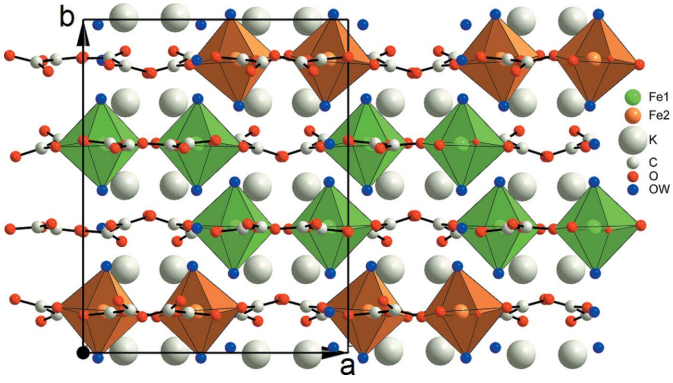

Figure 3
Succession of the slabs along the direction *b*.

3.2. Rietveld refinement of the mixed powder

The Rietveld refinement of the diffraction pattern obtained after the synthesis converges satisfactorily towards R_{Bragg} = 14% with the phase model obtained on a single crystal (Fig. 5). The parameters of the refinement are given in Table S2. The

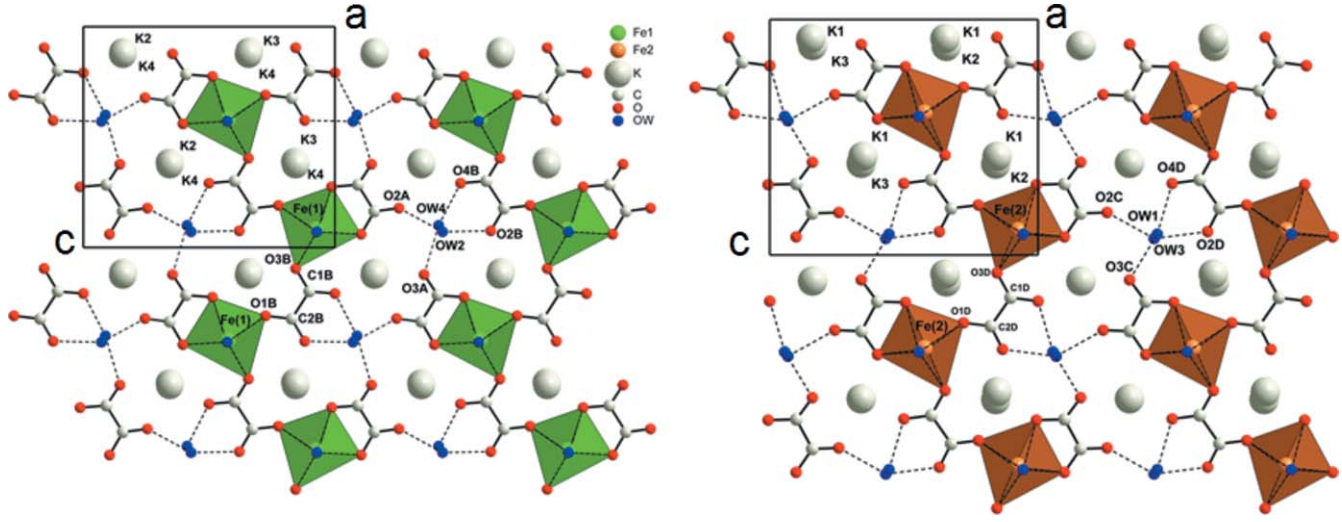

Figure 4
Individual slabs containing Fe(1) (left-hand view) and Fe(2) (right-hand view) sites and hydrogen bonding (dashed lines).

mixture contains approximately 76 (4) wt% (70% calc.) and 24 (4) wt% (30% calc) of phase 1 and KCl, respectively.

3.3. ^{57}Fe Mössbauer spectroscopy and magnetic susceptibility

The room temperature ^{57}Fe Mössbauer spectrum of the mixed powder is shown on Fig. 6. It can be fitted with two doublets of equal proportion with hyperfine parameters (δ = + 1.19 mm s^{-1}; Δ = 2.52 mm s^{-1} and δ = + 1.22 mm s^{-1}; Δ = 2.63 mm s^{-1}) characteristic of high-spin Fe^{2+} in octahedral oxygen environment (Greenwood & Gibb, 1971), in agreement with crystallographic results. The best fit is obtained by considering a third and broad doublet, representing *ca* 10% of the total resonant area, that probably arises from a Fe^{2+}-based unidentified impurity.

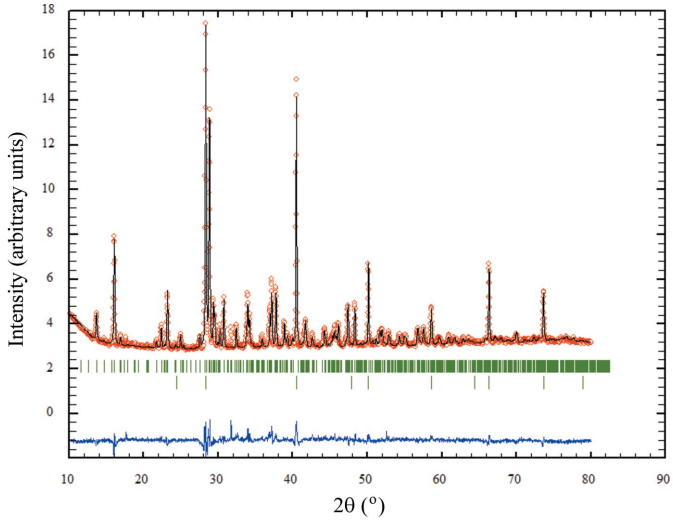

Figure 5
Final Rietveld plot for the mixing of $K_2[Fe^{II}(C_2O_4)_2(H_2O)_2]\cdot 0.18H_2O$ + 2KCl. Observed intensities are indicated by dots, the best-fit profile (upper trace) and the difference pattern (lower trace) are solid lines. The vertical bars correspond to the positions of the Bragg peaks for both phases.

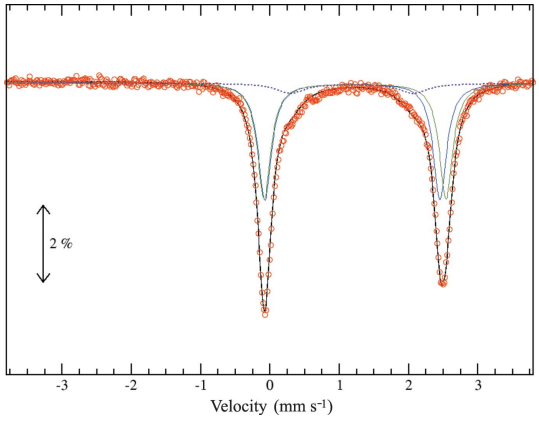

Figure 6
Mossbauer spectrum for mixed phases $K_2[Fe^{II}(C_2O_4)_2(H_2O)_2]\cdot 0.18H_2O$, 2KCl at room temperature.

Fig. 7 displays the temperature dependence of the magnetic susceptibility of the mixed powder recorded upon cooling in an applied field of 10 kOe in the 2–300 K temperature range. No magnetic transition is detected: $K_2[Fe^{II}(C_2O_4)_2(H_2O)_2]\cdot 0.18H_2O$ is paramagnetic down to 2 K. The reciprocal susceptibility (χ^{-1}) is linear and can be fitted with a Curie–Weiss law that yields a paramagnetic Curie temperature of $\theta p \simeq -4$ K, pointing out the weakness of the interactions. Assuming 25% of KCl in the mixed powder (see Section 3.2), the fit yields an effective moment μ_{eff} = 4.92 μ_B, which agrees with high-spin Fe^{2+} with an almost fully quenched orbital moment.

3.4. Comparison with other iron(II)-based oxalate structures and magnetic properties

The five iron(II) oxalate compounds reported in the literature are listed in Table 4.

In contrast to the target system $(NH_4)_2[Fe^{II}(C_2O_4)_2]\cdot H_2O$ (space group *P*321), the so-obtained compound, even though it has a similar chemical formula, contains metal-coordinating water molecules, which clearly differentiate the two structures and consequently the magnetic behaviors. The coordinated

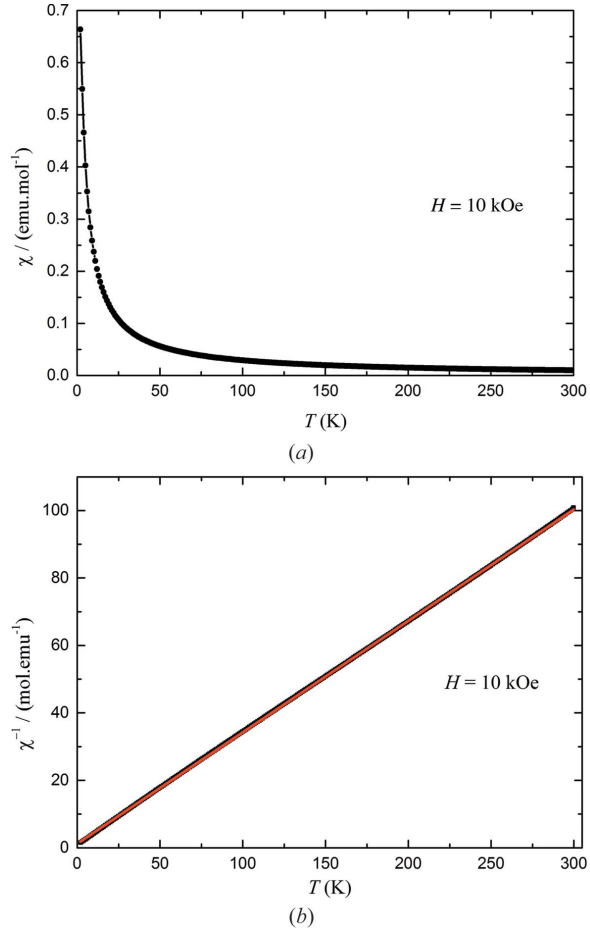

Figure 7
(*a*) Magnetic susceptibility of $K_2[Fe^{II}(C_2O_4)_2(H_2O)_2]\cdot 0.18H_2O$ and (*b*) the inverse of susceptibility $1/\chi$ between 2 and 300 K.

Table 4
Composition, crystallographic parameters and magnetic properties of ferrous oxalates.

CSD entry code or CCDC number	Ref.	Formula	Space group	*a* (Å)	*b* (Å)	*c* (Å)	*β* (°)	Magnetic properties
OXALFE01/OXALFE09	(a)	$Fe^{II}(ox)\cdot 2H_2O$	*Cccm*	12.260	5.570	15.48		Long-range AF order at T_N = 16 K
OXALFE07	(a)	$Fe^{II}(ox)\cdot 2H_2O$	*C*2/*c*	11.980	5.550	9.991	128.47	
SUKHAJ	(b)	$(NH_4)_2[Fe^{II}(ox)_2]\cdot H_2O$	*P*321	10.206 (1)		7.377 (1)		θp = −5.87 K. Weak exchange
ZOTTEJ	(b)	$K_4Na_2[Fe^{II}(ox)_2]_3\cdot 3H_2O$	*P*321	10.278		7.461		
This work	(c)	$K_2[Fe^{II}(ox)_2(H_2O)_2]\cdot 0.18H_2O$	*Pca*2$_1$	12.0251	15.1352	10.5524		2–300 K, paramagnetic θp $\simeq$ −4 K
BEMPIT-215206	(d)	$K_2Fe^{II}(ox)_2$	*P*2/*c*	8.521 (5)	6.885 (5)	14.691 (5)	93.811 (5)	T_N = 18 K, low-dimensional AF
1862164	(e)	$Na_2Fe^{II}{}_2(ox)_3\cdot 2H_2O$	*P*2$_1$/*c*	5.864 (4)	15.723 (6)	6.963 (3)	100.36 (4)	No magnetic ground state down to 2 K, strong magnetic exchange along the rungs of the two-leg ladder

References: (*a*) Chen *et al.* (1985), (*b*) Li *et al.* (2015), (*c*) this work, (*d*) Hursthouse *et al.* (2004), (*e*) Kreitlow *et al.* (2004).

water comes from the water molecules of the hydrated initial salts. The solvent-free synthesis at 200°C for the former leads to a compound containing insertion water (one water molecule per form unit) and therefore not fitting into the coordination sphere of the metal, whereas the structural formula of the latter $K_2[Fe^{II}(C_2O_4)_2(H_2O)_2]\cdot 0.18H_2O$ shows two coordination water molecules and $0.18H_2O$ insertion water molecules. This new divalent Fe oxalate compound could be obtained under mild conditions as it was possible to maintain the reducing atmosphere and prevent the oxidation of Fe^{II} to Fe^{III}.

It is interesting to relate the structural and magnetic properties of these iron oxalates, and in particular to the type of connection of the coordination O-polyhedra around the metal (see Fig. 8). In $Fe^{II}(ox)\cdot 2H_2O$ (*Cccm* OXALFE01/OXALFE09) or (*C*2/*c* OXALFE07) the $Fe^{II}O_4\cdot(H_2O)_2$ octahedra are linked by the oxalate tetradentate molecules and form chains according to the $\eta^1:\eta^1:\eta^1:\eta^1:\mu_2$ connection mode.

In $(NH_4)_2[Fe^{II}(C_2O_4)_2]\cdot H_2O$ (*P*321 SUKHAJ) or $K_4Na_2[Fe^{II}(C_2O_4)_2]_3\cdot 3H_2O$ (*P*321 ZOTTEJ), the triangular iron(II) units are obtained by the particular $\eta^1:\eta^1:\eta^1:\eta^1:\mu_3$ connection in the hexagonal plane of the structure with a $Fe^{II}O–C–O–Fe^{II}$ magnetic super-exchange path. The magnetic exchange is weak in these planes with AF interactions and probably magnetic frustration. Between the planes, the bidendate $\eta^1:\eta^0:\eta^1:\eta^0:\mu_2$ connection gives a longer Fe^{II}–O–C–C–O–Fe^{II} exchange path that probably causes little or no interaction.

4. Conclusion

Using solvent-free synthesis, we have discovered $K_2Fe[(C_2O_4)_2(H_2O)_2]\cdot 0.18H_2O$, a new member of the family of iron oxalates. The crystal structure of this new hydrated iron oxalate compound could be fully determined from single crystal and powder X-ray diffraction data. The structure of the title compound is distinct from that of the five Fe^{II}-oxalate solid hybrids reported to date. ^{57}Fe Mössbauer spectroscopy confirms the presence of divalent iron in agreement with crystallographic results. Magnetic measurements demonstrates that $K_2Fe[(C_2O_4)_2(H_2O)_2]\cdot 0.18H_2O$ exhibits paramagnetic behavior down to 2 K.

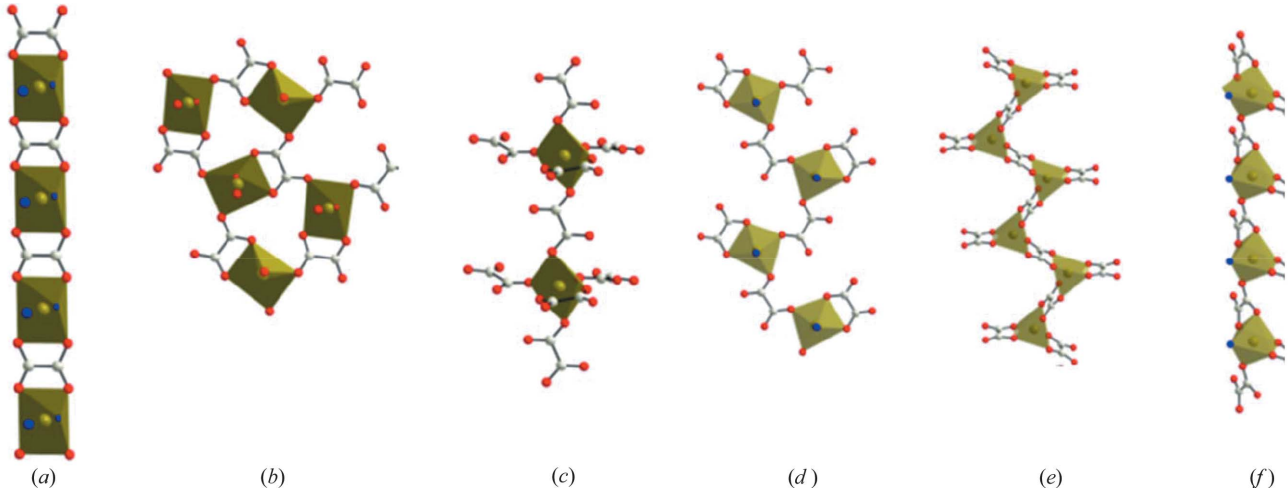

Figure 8
Connection of $Fe^{II}O_6$ polyhedra by the oxalates in (*a*) $Fe^{II}(ox)\cdot 2H_2O$ $\eta^1:\eta^1:\eta^1:\eta^1:\mu_2$, (*b*) $(NH_4)_2[Fe(II)(C_2O_4)_2]\cdot H_2O$ within the planes $\eta^1:\eta^1:\eta^1:\eta^1:\mu_3$ between the hexagonal planes of the structure $\eta^1:\eta^0:\eta^1:\eta^0:\mu_2$, (*c*) $K_2[Fe^{II}(C_2O_4)_2(H_2O)_2]\cdot 0.18H_2O$ $\eta^1:\eta^0:\eta^1:\eta^0:\mu_2$, (*d*) $K_2Fe^{II}(ox)_2$, $\eta^1:\eta^1:\eta^1:\eta^1:\mu_2$ and $\eta^1:\eta^1:\eta^0:\eta^0:\mu_1$, (*e*) $Na_2Fe^{II}{}_2(ox)_3(H_2O)_2$ $\eta^1:\eta^1:\eta^1:\eta^0:\mu_2$ and (*f*) $\eta^1:\eta^1:\eta^0:\eta^0:\mu_1$.

References

Blatov, V. A., Carlucci, L., Ciani, G. & Proserpio, D. M. (2004). *CrystEngComm*, **6**, 377–395.

Brandenburg, K. & Putz, H. (1997). *Diamond*. Crystal Impact, 53227 Bonn, Germany. https://www.crystalimpact.de/diamond.

Bruker (2004). *APEX2*, *SAINT* and *SADABS*. Bruker AXS Inc., Madison, Wisconsin, USA.

Chen, J. Y., Simizu, S. & Friedberg, S. A. (1985). *J. Appl. Phys.* **57**, 3338–3340.

Coronado, E., Galán-Mascarós, J. R., Gómez-García, C. J. & Martínez-Agudo, J. M. (1999). *Adv. Mater.* **11**, 558–561.

García-Couceiro, U., Castillo, O., Luque, A., García-Terán, J. P., Beobide, G. & Román, P. (2006). *Cryst. Growth Des.* **6**, 1839–1847.

Greenwood, N. N. & Gibb, T. C. (1971). *Mössbauer Spectroscopy*, pp. 87–111. Netherlands: Springer.

Groom, C. R., Bruno, I. J., Lightfoot, M. P. & Ward, S. C. (2016). *Acta Cryst.* B**72**, 171–179.

Hursthouse, M. B., Light, M. E. & Price, D. J. (2004). *Angew. Chem. Int. Ed.* **43**, 472–475.

Krause, L., Herbst-Irmer, R., Sheldrick, G. M. & Stalke, D. (2015). *J. Appl. Cryst.* **48**, 3–10.

Kreitlow, J., Baabe, D., Wolter, A. U. B., Süllow, S., Litterst, F. J., Price, D. J. & Klauss, H.-H. (2004). *J. Magn. Magn. Mater.* **272–276**, 152–153.

Lhotel, E., Simonet, V., Ortloff, J., Canals, B., Paulsen, C., Suard, E., Hansen, T., Price, D. J., Wood, P. T., Powell, A. K. & Ballou, R. (2013). *Eur. Phys. J. B*, **86**, 248.

Li, H., Eddaoudi, M., O'Keeffe, M. & Yaghi, O. M. (1999). *Nature*, **402**, 276–279.

Li, J. H., Liu, H., Wei, L. & Wang, G. M. (2015). *Solid State Sci.* **48**, 225–229.

Mínguez Espallargas, G. & Coronado, E. (2018). *Chem. Soc. Rev.* **47**, 533–557.

Moessner, R. & Ramirez, A. P. (2006). *Phys. Today*, **59**, 24–29.

Petříček, V., Dušek, M. & Palatinus, L. (2014). *Z. Kristallogr. Cryst. Mater.* **229**, 345–352.

Rodríguez-Carvajal, J. (2011). *FullProf Suite 2011*, Version 2.05. LLB, CEA/ Saclay, France.

Shannon, R. D. (1976). *Acta Cryst.* A**32**, 751–767.

Shannon, R. D. & Prewitt, C. T. (1969). *Acta Cryst.* B**25**, 925–946.

Sheldrick, G. M. (2008). *Acta Cryst.* A**64**, 112–122.

Sheldrick, G. M. (2015). *Acta Cryst.* C**71**, 3–8.

Tamaki, H., Zhong, Z. J., Matsumoto, N., Kida, S., Koikawa, M., Achiwa, N., Hashimoto, Y. & Okawa, H. (1992). *J. Am. Chem. Soc.* **114**, 6974–6979.

Wang, X., Kurono, R., Nishimura, S.-I., Okubo, M. & Yamada, A. (2015). *Chem. Eur. J.* **21**, 1096–1101.

Zhao, J.-P., Han, S.-D., Jiang, X., Xu, J., Chang, Z. & Bu, X.-H. (2015). *Chem. Commun.* **51**, 4627–4630.